Electronic Spectra, Optical Activity, and Crystal-Field Energy-Level Structure of Dy^{3+} in Trigonal $Na_3[Dy(oda)_3]\cdot 2NaClO_4\cdot 6H_2O$ Crystals†

David H. Metcalf, Todd A. Hopkins, and F. S. Richardson*

Department of Chemistry, University of Virginia, Charlottesville, Virginia 22901

Received March 31, 1995®

Optical absorption and emission measurements are used to locate and assign 152 crystal-field energy levels split out of the $4f^9$ electronic configuration of Dy^{3+} in $Na_3[Dy(oda)_3]\cdot 2NaClO_4\cdot 6H_2O$ (where oda denotes an oxydiacetate ligand). The absorption measurements span the 230−1800 nm wavelength range, and they encompass all optical transitions that may occur between the $^6H_{15/2}$ *ground* multiplet and 63 different *excited* multiplet manifolds of the $4f^9(Dy^{3+})$ electronic configuration. The emission measurements span the 470−900 nm wavelength range, and they encompass all transitions that originate within the $^4F(3)_{9/2}$ excited multiplet manifold (centered at ca. 21 100 cm^{-1} above ground) and terminate on levels split out of the ^6H_J ($J = {}^{15}/_2, {}^{13}/_2, {}^{11}/_2, {}^{9}/_2$, and ${}^{7}/_2$) and ^6F_J ($J = {}^{11}/_2, {}^{9}/_2$) multiplet manifolds of $4f^9(Dy^{3+})$. The combined absorption and emission measurements provide access to the energy-level structures of 65 $4f^9[SL]J$ multiplet manifolds of Dy^{3+} (*all* multiplet manifolds with baricenter energies <43 000 cm^{-1} above ground). The site symmetry of Dy^{3+} ions in $Na_3[Dy(oda)_3]\cdot 2NaClO_4\cdot 6H_2O$ is D_3, and all crystal-field levels split out of the $4f^9(Dy^{3+})$ electronic configuration are Kramers doublets with either E′ or E″ symmetry in the D_3 double-rotation group. Among the 348 crystal-field levels predicted for the 65 multiplet manifolds examined in this study, 152 are both located *and* assigned (with respect to crystal-field symmetry type, E′ or E″, and principal $[SL]J$ multiplet parentage). Symmetry assignments are based on results obtained from both *linearly* and *circularly polarized* absorption and emission measurements. The 152 assigned levels are analyzed in terms of a model Hamiltonian that includes consideration of both isotropic and non-isotropic 4f-electron/crystal-field interactions, and the interaction parameters derived from this analysis are discussed and then compared with those obtained for other $Na_3[Ln(oda)_3]\cdot 2NaClO_4\cdot 6H_2O$ systems *and* for Dy^{3+} in other crystalline hosts. The parametrized form of the model Hamiltonian derived from the energy-level analysis yields calculated-to-experimental data fits with an rms deviation of 8.2 cm^{-1} (between calculated and observed energies). Several multiplet-to-multiplet transition regions of Dy^{3+} in $Na_3[Dy(oda)_3]\cdot 2NaClO_4\cdot 6H_2O$ exhibit strong chiroptical activity, and the circular dichroism and circularly polarized luminescence spectra observed in these regions are presented and discussed. Quantitatively determined line strengths are reported for 39 of the transitions observed in the *unpolarized* axial absorption spectra.

Introduction

The isomorphous series of compounds $Na_3[Ln(oda)_3]\cdot 2NaClO_4\cdot 6H_2O$ (where Ln^{3+} denotes a trivalent lanthanide ion and oda denotes an oxydiacetate ligand) are excellent model systems for examining the effects of a structurally complex ligand environment on lanthanide $4f^N$ electronic state structure and optical properties. Optical-quality single crystals of these compounds are readily grown from aqueous solution, and at room temperature the crystals belong to the space group $R32$.[1-3] The Ln^{3+} ions are located at sites with D_3 symmetry, and each Ln^{3+} ion is coordinated to three oxydiacetate ($C_4H_4O_5^{2-} \equiv {}^-OOCCH_2OCH_2COO^-$) ligands to form a tris-terdentate chelate structure of trigonal-dihedral (D_3) point-group symmetry. The LnO_9 coordination cluster in each $Ln(oda)_3^{3-}$ complex forms a slightly distorted tricapped trigonal-prism polyhedron (of D_3 symmetry), with the top and bottom triangles defined by carboxylate oxygen atoms and the capping positions (on normals to the rectangular faces) occupied by ether oxygen atoms. The backbone of each bicyclic Ln(oda) chelate ring system is nearly planar and stretches diagonally across a rectangular face on the LnO_9 trigonal-prism structure. The chelate rings contain highly anisotropic charge distributions, and their interactions with the lanthanide 4f electrons produce effects not ordinarily observed in structurally simpler systems. Furthermore, single crystals of $Na_3[Ln(oda)_3]\cdot 2NaClO_4\cdot 6H_2O$ grow (spontaneously) in two enantiomorphic forms, which differ with respect to the absolute configuration of their constituent $Ln(oda)_3^{3-}$ complexes and the chiral (left-handed or right-handed) arrangement of these complexes about the trigonal symmetry axis of the crystal.[4] Therefore, these systems exhibit *chiroptical* properties that may be exploited in characterizing spectroscopic state structure and transition mechanisms.[5,6]

The optical and chiroptical properties of $Na_3[Ln(oda)_3]\cdot 2NaClO_4\cdot 6H_2O$ systems have been studied extensively, at various levels of experimental characterization and theoretical analysis. The most thorough studies have been reported for the neodymium,[7-10] samarium,[10-14] europium,[15-18] gadolinium,[19-21]

* Author to whom correspondence should be addressed.
† oda ≡ oxydiacetate ($^-OOCCH_2OCH_2COO^-$).
® Abstract published in *Advance ACS Abstracts,* August 1, 1995.

(1) Albertsson, J. *Acta. Chem. Scand.* **1968**, *22*, 1563.
(2) Albertsson, J. *Acta. Chem. Scand.* **1970**, *24*, 3527.
(3) Albertsson, J.; Elding, I. *Acta. Chem. Scand., Ser. A* **1977**, *31*, 21.
(4) Fronczek, F. R.; Banerjee, A. K.; Watkins, S. F.; Schwartz, R. W. *Inorg. Chem.* **1981**, *20*, 2745.
(5) Richardson, F. S.; Faulkner, T. R. *J. Chem. Phys.* **1982**, *76*, 1595.
(6) Richardson, F. S. *J. Less-Common Met.* **1989**, *149*, 161.
(7) Vala, M.; Szczepanski, J.; Banerjee, A. K.; Chowdhury, M. *Chem. Phys.* **1989**, *134*, 149.
(8) May, P. S.; Jayasankar, C. K.; Richardson, F. S. *Chem. Phys.* **1989**, *138*, 123.
(9) May, P. S.; Jayasankar, C. K.; Richardson, F. S. *Chem. Phys.* **1989**, *138*, 139.
(10) May, P. S. Ph.D. Dissertation, University of Virginia, 1988.
(11) May, P. S.; Reid, M. F.; Richardson, F. S. *Mol. Phys.* **1987**, *61*, 1455.
(12) May, P. S.; Reid, M. F.; Richardson, F. S. *Mol. Phys.* **1987**, *61*, 1471.

0020-1669/95/1334-4868$09.00/0

holmium,[22-24] and erbium[25,26] members of the series. These studies included detailed measurements and analysis of crystal-field energy-level structure, optical and chiroptical line strengths, and transition polarization properties, and they have provided important new insights into the detailed nature of 4f-electron/ligand-field interactions in a highly anisotropic ligand environment. The latter are of significant interest in the development of theories and models that may be used to rationalize, calculate, and/or predict the $4f^N$ electronic state structure and optical properties of lanthanide ions in structurally complex systems.[27-32]

In the present paper, we report results obtained from optical and chiroptical absorption and emission measurements on $Na_3[Dy(oda)_3]\cdot 2NaClO_4\cdot 6H_2O$, and we also report the first detailed crystal-field analysis of the $4f^9(Dy^{3+})$ electronic energy-level structure in this system (denoted hereafter by DyODA). The absorption measurements span the 230−1800 nm wavelength range, and they encompass all transitions that may occur between the $^6H_{15/2}$ *ground* multiplet and 63 different *excited* multiplet manifolds of the $4f^9(Dy^{3+})$ electronic configuration. The emission measurements span the 470−900 nm wavelength range, and they encompass all transitions that originate within the $^4F(3)_{9/2}$ excited multiplet manifold (centered at ca. 21 100 cm^{-1} above ground) and terminate on levels split out of the ^6H_J ($J = {}^{15}/_2, {}^{13}/_2, {}^{11}/_2, {}^{9}/_2, {}^{7}/_2$) and ^6F_J ($J = {}^{11}/_2, {}^{9}/_2$) multiplet manifolds of $4f^9(Dy^{3+})$.

The optical absorption and emission experiments carried out in this study included intensity measurements of light propagating either along or perpendicular to the unique (optic) axis of a DyODA crystal. Measurements performed along this axis are referred to hereafter as *axial* (α) measurements, and those performed perpendicular to this axis are referred to as *orthoaxial* measurements. Two types of *axial* measurements were performed in both the absorption and emission experiments: one in which unpolarized light intensities were measured and one in which differential, left- *versus* right-circularly polarized light intensities were measured. The latter are referred to as *circular dichroism* (CD) measurements in the absorption experiments and as *circularly polarized luminescence* (CPL) measurements in the emission experiments.[6,33,34] In the *orthoaxial* absorption and emission experiments, intensities were measured for *linearly* polarized light in which the electric-field vector (**E**) was aligned either perpendicular (σ-polarized) or parallel (π-polarized) to the optic axis of the crystal.

In D_3 symmetry, all crystal-field levels split out of the $4f^9$ electronic configuration of Dy^{3+} are Kramers doublets, and each may be classified as having either E′ or E″ symmetry in the D_3 double-rotation group ($\bar{D}_3$), where E′ and E″ denote irreducible representation (irrep) labels in this group. Among the 348 crystal-field levels split out of the 65 lowest-energy $^{2S+1}L_J$ multiplet manifolds of $4f^9(Dy^{3+})$, 152 were located and assigned from our combined absorption and emission measurements. This represents the largest number of crystal-field levels located and assigned for any $Na_3[Ln(oda)_3]\cdot 2NaClO_4\cdot 6H_2O$ system, and it provides an excellent basis for carrying out a detailed analysis of $4f^9(Dy^{3+})$ electronic state structure in DyODA. In the present study, we analyzed the observed energy-level data in terms of a model Hamiltonian constructed to represent all the major interactions expected to contribute to $4f^9(Dy^{3+})$ energy-level structure in DyODA. A parametrized form of this model Hamiltonian is used to perform parametric fits to calculated-to-observed energy-level data, and these fits yield an rms deviation of 8.2 cm^{-1} between the calculated and experimentally determined energies of the 152 assigned crystal-field levels. The quality of these data fits is rather remarkable, given the large number of different [*SL*]*J* multiplet manifolds represented in the energy-level data set, and the Hamiltonian parameter values derived from these data fits are well characterized.

All of the absorption and emission measurements on DyODA were carried out at sample temperatures of 15 and 295 K. The spectra obtained at 295 K are very congested and difficult to analyze due to the presence of innumerable "hot" bands. At 295 K, seven of the eight crystal-field levels split out of the $^6H_{15/2}$ (ground) multiplet have significant thermal populations, and transitions from each of these levels contribute to the 295 K absorption spectra. In the 295 K emission spectra, transitions are observed from four of the five crystal-field levels split out of the $^4F(3)_{9/2}$ (emitting) multiplet. At 15 K, only three levels of $^6H_{15/2}$ are thermally populated and contribute to the absorption spectra, and only one level of $^4F(3)_{9/2}$ contributes to the emission spectra. In regions where it is possible to compare the 15 and 295 K spectra on a line-by-line (or transition-by-transition) basis, the results, indicate that both the locations and symmetries of the crystal-field levels are essentially the same at 15 and 295 K. The detailed energy-level analyses reported in this paper are based entirely on data obtained at 15 K.

Experimental Section

Single crystals of $Na_3[Dy(oda)_3]\cdot 2NaClO_4\cdot 6H_2O$ were grown from aqueous solution by following the methods of Albertsson.[1,2] Damp Whatman glass-microfiber filter paper was used to polish crystals to a thickness and shape suitable for optical measurements. Crystal samples were mounted on a one-piece copper mount using Crycon grease and indium foil, and the copper mount was attached to the cold head of a CTI-Cryogenics closed-cycle helium refrigerator/cryostat, with strips of indium providing a thermally conductive interface. Cold-head temperature was controlled using a Lake Shores temperature controller (Model DRC-70).

All absorption and circular dichroism (CD) measurements performed over the 230−480 nm wavelength range were carried out using a high-resolution spectrophotometer constructed in this laboratory. The dispersing element in this instrument is a 0.75 m double-grating monochromator and spectral resolutions < 0.1 nm could be achieved

(13) May, P. S.; Reid, M. F.; Richardson, F. S. *Mol. Phys.* **1987**, *62*, 341.
(14) May, P. S.; Metcalf, D. H.; Richardson, F. S.; Carter, R. C.; Miller, C. E.; Palmer, R. A. *J. Lumin.* **1992**, *51*, 249.
(15) Berry, M. T.; Schwieters, C.; Richardson, F. S. *Chem. Phys.* **1988**, *122*, 105.
(16) Berry, M. T.; Schwieters, C.; Richardson, F. S. *Chem. Phys.* **1988**, *122*, 125.
(17) May, P. S.; Richardson, F. S. *Chem. Phys. Lett.* **1991**, *179*, 277.
(18) Görller-Walrend, C.; Verhoeven, P.; D'Olieslager, J.; Fluyt, L.; Binnemans, K. *J. Chem. Phys.* **1994**, *100*, 815.
(19) Kundu, T.; Banerjee, A. K.; Chowdhury, M. *Phys. Rev. B* **1990**, *41*, 10911.
(20) Stephens, E. M.; Metcalf, D. H.; Berry, M. T.; Richardson, F. S. *Phys. Rev. B* **1991**, *44*, 9895.
(21) Kundu, T.; Banerjee, A. K.; Chowdhury, M. *Chem. Phys.* **1991**, *156*, 95.
(22) Moran, D. M.; De Piante, A.; Richardson, F. S. *Phys. Rev. B* **1990**, *42*, 3317.
(23) Moran, D. M.; Richardson, F. S. *Phys. Rev. B* **1990**, *42*, 3331.
(24) Moran, D. M.; Richardson, F. S. *Inorg. Chem.* **1992**, *31*, 813.
(25) Schoene, K. A.; Quagliano, J. R.; Richardson, F. S. *Inorg. Chem.* **1991**, *20*, 3803.
(26) Schoene, K. A. Ph.D. Dissertation, University of Virginia, 1989.
(27) Reid, M. F.; Richardson, F. S. *J. Chem. Phys.* **1983**, *79*, 5735.
(28) Reid, M. F.; Richardson, F. S. *J. Phys. Chem.* **1984**, *88*, 3579.
(29) Dallara, J. J.; Reid, M. F.; Richardson, F. S. *J. Phys. Chem.* **1984**, *88*, 3587.
(30) Richardson, F. S.; Berry, M. T.; Reid, M. F. *Mol. Phys.* **1986**, *58*, 929.
(31) Stephens, E. M.; Reid, M. F.; Richardson, F. S. *Inorg. Chem.* **1984**, *23*, 4611.
(32) Devlin, M. T.; Stephens, E. M.; Richardson, F. S. *Inorg. Chem.* **1988**, *27*, 1517.
(33) Riehl, J. P.; Richardson, F. S. *Chem. Rev.* **1986**, *86*, 1.
(34) Crosswhite, H. M.; Crosswhite, H. *J. Opt. Soc. Am. B* **1984**, *1*, 246.

in both the absorption and CD spectra recorded between 230 and 480 nm. Absorption spectra between 480 and 1800 nm were obtained using a commercial Cary Model 2415 UV/vis/near-IR spectrophotometer. All the quantitative line-strength data reported in this paper are for transitions observed in absorption spectra at wavelengths < 480 nm.

All of the optical emission measurements performed in this study were carried out using instrumentation constructed *in-house*. The excitation source was an argon ion laser (Innova Model 90-6UV), the emission dispersing element was a 0.75 m double-grating monochromator, and the emission detector system was an RCA Model C31034 PMT with associated photon-counting electronics. A Hinds International Model PEM-80 photoelastic modulator was used as a polarization discriminator in our *linearly* and *circularly* polarized emission intensity measurements. Excitation was at either 454.5 or 476.5 nm, corresponding to either $^6H_{15/2} \rightarrow {}^4I(3)_{15/2}$ or $^6H_{15/2} \rightarrow {}^4F(3)_{9/2}$ absorptive transitions. These two excitation modes yield identical emission spectra, all of which can be assigned to transitions that originate from crystal-field levels of the $^4F(3)_{9/2}$ multiplet. Emission spectra recorded over the 470−900 nm wavelength range span all transitions that originate from $^4F(3)_{9/2}$ and terminate on levels split out of the ^6H_J ($J = {}^{15}/_2, {}^{13}/_2, {}^{11}/_2, {}^9/_2, {}^7/_2$) and ^6F_J ($J = {}^{11}/_2, {}^9/_2$) multiplet manifolds.

Optical Selection Rules and Line Assignments

It was noted earlier, in the Introduction, that all crystal-field levels split out of the $4f^9$ electronic configuration of Dy^{3+} in DyODA are Kramers doublets with either E′ or E″ symmetry in the D_3 double-rotation group (denoted here by $\bar{D}_3$). If the state vectors of these levels are expressed in a JM_J angular-momentum basis, those that contain $M_J = \pm{}^1/_2, \pm{}^5/_2$ (mod 3) components transform as the E′ irreducible representation (irrep) of the $\bar{D}_3$ double-group, whereas those that contain $M_J = \pm{}^3/_2$ (mod 3) components transform as the E″ irrep of $\bar{D}_3$. All transitions between crystal-field levels in DyODA may be classified (by symmetry) as E′ ↔ E′, E′ ↔ E″, or E″ ↔ E″. Optical selection rules for each of these transition types depend on the polarization properties of the perturbing radiation field and on the interaction mechanisms responsible for the transitions.

All transitions observed in the optical absorption and emission of DyODA may be presumed to occur via electric- and/or magnetic-dipole interaction mechanisms, and the relevant interaction operators for connecting crystal-field states are the electric ($\hat{\boldsymbol{\mu}}$) and magnetic ($\hat{\mathbf{m}}$) dipole moment operators. Here we define the $\hat{\boldsymbol{\mu}}$ and $\hat{\mathbf{m}}$ operators to be located at Dy^{3+} sites in the DyODA crystal and express their components ($\hat{\mu}_q$ and $\hat{m}_q$) in a spherical coordinate system with $q = 0, \pm 1$. At any given site, the $q = 0$ axis is defined to be coincident with the trigonal symmetry axis of a $Dy(oda)_3^{3-}$ complex and parallel to the unique (optic) axis of the crystal. The $\hat{\mu}_0$ and $\hat{m}_0$ operators transform as the A_2 irrep under the symmetry operations of the $\bar{D}_3$ double-group, and the $\hat{\mu}_{\pm 1}$ and $\hat{m}_{\pm 1}$ operators transform as the E irrep under the symmetry operations of this group.

Given the symmetry properties described above for the crystal-field states and the $\hat{\mu}_q$ and $\hat{m}_q$ operators, selection rules for each of the E′ ↔ E′, E′ ↔ E″, and E″ ↔ E″ transition types are easily derived. According to these selection rules, the $\hat{\mu}_0$ and $\hat{m}_0$ operators can only connect states of identical symmetry (E′ with E′ or E″ with E″), whereas the $\hat{\mu}_{\pm 1}$ and $\hat{m}_{\pm 1}$ operators can make E′ ↔ E′ and E′ ↔ E″ connections, but not E″ ↔ E″ connections. Applications of these selection rules to the *axial* and σ- and π-polarized *orthoaxial* measurement configurations used in our optical experiments are shown in Table 1.

We note from Table 1 that the selection rules for E″ ↔ E″ transitions are more restrictive than those for E′ ↔ E′ and E′ ↔ E″ transitions, and generally, E″ ↔ E″ transitions can be readily identified from comparisons of axial and orthoaxial spectra. However, unambiguous assignments of E′ ↔ E′ and E′ ↔ E″ transition types are possible only if the transitions are known (or assumed) to have *either* predominantly electric-dipole *or* predominantly magnetic-dipole character. In nearly all of the transition regions examined in this study, electric-dipole contributions to line strength are expected to be much greater than magnetic-dipole contributions, and observed σ- *versus* π-polarized intensity ratios may be used to distinguish between E′ ↔ E′ and E′ ↔ E″ transition types.

The axial selection rules given in Table 1 apply to both the *unpolarized* axial absorption and emission measurements and all of the *chiroptical* (CD and CPL) measurements performed in this study. However, whereas the transition intensities observed in the unpolarized spectra reflects *sums* of electric- and magnetic-dipole line strengths (either of which may be vanishingly small), the CD or CPL intensity of any given transition is determined by a *product* of electric- and magnetic-dipole transition amplitudes.[5,6,30] For an absorptive transition A → B, the unpolarized axial line strength may be written as

Table 1. Electric (μ) and Magnetic (m) Dipole Selection Rules for Optical Absorption and Emission Transitions in $Na_3[Dy(oda)_3]\cdot 2NaClO_4\cdot 6H_2O$

		orthoaxial spectra[c]	
transition[a]	axial spectra[b]	σ-polarized	π-polarized
E′ ↔ E′	$\mu_{\pm 1}; m_{\pm 1}$	$\mu_{\pm 1}; m_0$	$\mu_0; m_{\pm 1}$
E′ ↔ E″	$\mu_{\pm 1}; m_{\pm 1}$	$\mu_{\pm 1}$	$m_{\pm 1}$
E″ ↔ E″	forbidden	m_0	μ_0

[a] Energy levels are labeled according to their irreducible representation (irrep) in the $\bar{D}_3$ double-group. [b] Light propagating along the crystallographic c axis (the *unique* axis), which is parallel to the trigonal symmetry axes of the $Dy(oda)_3^{3-}$ complexes. [c] Light propagating along a direction orthogonal to the crystallographic c axis.

$$S_{AB}(\alpha) = {}^1/_2\left|\sum_q \sum_{a,b}\langle A_a|\hat{\mu}_q|B_b\rangle\right|^2 + {}^1/_2\left|\sum_q \sum_{a,b}\langle A_a|\hat{m}_q|B_b\rangle\right|^2 \quad (1)$$

where $q = \pm 1$, and the summations $\sum_{a,b}$ are over the degenerate components of levels A and B. The corresponding circular dichroic (CD) line strength is given by

$$R_{AB}(\alpha) = {}^3/_2\,\mathrm{Im}\sum_q \sum_{a,b}\langle A_a|\hat{\mu}_q|B_b\rangle\langle A_a|\hat{m}_q|B_b\rangle^* \quad (2)$$

where $q = \pm 1$, Im signifies the imaginary part of the quantity that follows, and the asterisk denotes complex conjugation. The R_{AB} quantity is generally called a transition *rotatory strength*, reflecting its relationship to optical rotatory power (the ability of an optically active substance to rotate the plane of polarization of linearly polarized light). Expressions identical to eqs 1 and 2 may be written for transitions observed in unpolarized axial emission spectra and in CPL spectra. Finally we note that whereas S_{AB} is a pure *scalar* quantity with values ≥ 0, R_{AB} is a *pseudoscalar* quantity with values that may be either positive or negative in sign, depending on whether the electric- and magnetic-dipole transition moments are *in-phase* or *180° out-of-phase*.

Calculations and Data Analysis

Energy Levels. The $4f^9$ electronic energy-level structure of Dy^{3+} in DyODA was analyzed in terms of a model Hamiltonian that may be written as

$$\hat{H} = \hat{H}_a + \hat{H}_{cf}^{+} \quad (3)$$

where $\hat{H}_a$ is defined to incorporate the isotropic parts of $\hat{H}$ (including the spherically symmetric parts of the 4f-electron/crystal-field interactions) and $\hat{H}_{cf}^{+}$ is defined to represent the non-spherically symmetric components of the *even-parity* crystal field. We refer to $\hat{H}_a$ as the *atomic* Hamiltonian and call $\hat{H}_{cf}^{+}$ the *crystal-field* Hamiltonian. In our model, the $\hat{H}_a$ operator is defined by

$$\hat{H}_a = E_{av} + \sum_k F^k f_K + \alpha\hat{L}(\hat{L}+1) + \beta\hat{G}(G_2) + \gamma\hat{G}(R_7) + \sum_i T^i\hat{t}_i + \zeta_{so}\hat{A}_{so} + \sum_k P^k\hat{Q}_k + \sum_j M^j\hat{m}_j \quad (4)$$

where $k = 2, 4, 6$; $i = 2, 3, 4, 6, 7, 8$; $j = 0, 2, 4$; and each of the interaction operators and parameters is written and defined according to conventional practice.[34,35]

The even-parity crystal-field Hamiltonian ($\hat{H}_{cf}^{+}$) is defined to reflect the D_3 site symmetry of the Dy^{3+} ions in DyODA and is

(35) Carnall, W. T.; Goodman, G. L.; Rajnak, K.; Rana, R. S. *J. Chem. Phys.* **1989**, *90*, 3443.

written as

$$\hat{H}_{cf}^{+} = \sum_{k,m} B_m^k \hat{U}_m^{(k)} \quad (5)$$

where $k = 2, 4, 6$; $m = 0, \pm3, \pm6$ (with $|m| \leq k$); $\hat{U}_m^{(k)}$ is an intraconfigurational unit-tensor operator of rank k and order m; and the B_m^k are crystal-field interaction parameters. The B_m^k parameters in eq 5 are interrelated according to $B_{-m}^k = (-1)^m B_m^k$, so this equation contains only six *independent* parameters. In the calculations reported here, the six independent B_m^k parameters were chosen to be B_0^2, B_0^4, B_3^4, B_0^6, B_3^6, and B_6^6.

Both the atomic and crystal-field Hamiltonians ($\hat{H}_a$ and $\hat{H}_{cf}^{+}$) are defined to operate entirely *within* the $4f^9$ electronic configuration of Dy^{3+}, though 12 of the 20 interaction terms in $\hat{H}_a$ represent effects due to *interconfigurational mixings* (between $4f^9$ and higher-energy configurations of like parity).[34,35] Our energy-level calculations were carried out in two steps. *First*, the atomic Hamiltonian was diagonalized within the *complete* basis of $f^9SM_SLM_L$ states (a total of 2002 states), with the parameters of $\hat{H}_a$ fixed at the values reported previously for Dy^{3+} in $LaCl_3$.[36] The 886 lowest-energy $f^9[SL]JM_J$ intermediate-coupled states derived from this calculation were then used as the basis set in our calculations of crystal-field energy-level structure. In these latter calculations, the *complete* model Hamiltonian ($\hat{H} = \hat{H}_a + \hat{H}_{cf}^{+}$) was diagonalized within the $f^9[SL]JM_J$ basis, with 22 of the 26 parameters in $\hat{H}$ treated as variables to fit calculated energy levels to experimentally observed energy-level data. Both the energies and symmetries of crystal-field levels were considered in performing these parametric data fits.

Transition Line Strengths. Among the transitions observed in the unpolarized axial absorption spectra of DyODA at 15 K, 39 were sufficiently well-resolved to permit quantitative determinations of line strength. Line strengths for these resolved transitions were determined by integrating observed absorbances over transition line profiles and then evaluating

$$S_{i\rightarrow f}(\alpha) = \frac{3.06 \times 10^{-3} g_i}{X_i(T)\, \chi_\lambda c_m b} \int_{i\rightarrow f} \frac{A(\bar{\nu})\, d\bar{\nu}}{\bar{\nu}} \quad (6)$$

where $S_{i\rightarrow f}(\alpha)$ denotes the unpolarized axial line strength of a transition $i \rightarrow f$, expressed in units of D^2 ($D \propto 1$ debye unit $= 10^{-18}$ esu cm $=$ 3.3356×10^{-30} C m); g_i is the degeneracy of level i; $X_i(T)$ is the fractional thermal (Boltzmann) population of level i at the sample temperature (T); c_m is the molar concentration of Dy^{3+} ions in DyODA; b is the sample thickness (in cm); χ_λ is a correction factor for bulk sample refractivity at the transition wavelength λ; $A(\bar{\nu})$ denotes the decadic absorbance of the sample at wavenumber $\bar{\nu}$; and the integration is over the absorbance profile of the $i \rightarrow f$ transition. The molar concentration of Dy^{3+} ions in DyODA is 2.168 ($c_m = 2.168$ mol/L); all crystal-field levels of Dy^{3+} in DyODA are doubly-degenerate (and, therefore, $g_i = 2$); and all of our unpolarized axial absorption measurements were performed on crystals of 0.155 cm thickness. With this information, eq 6 may be rewritten as

$$S_{i\rightarrow f}(\alpha) = \frac{0.0182}{X_i(T)\, \chi_\lambda} \int_{i\rightarrow f} \frac{A(\bar{\nu})\, d\bar{\nu}}{\bar{\nu}} \quad (7)$$

All line-strength determinations were for transitions that originate from either the ground or first excited crystal-field levels of the $^6H_{15/2}$ (ground) multiplet of Dy^{3+} ($4f^9$). At 15 K, the X_i thermal population factors for these levels are 0.83 for the ground level and 0.15 for the first excited level (located at 18 cm^{-1} above ground). Refractive index dispersion data for $Na_3[Ln(oda)_3]\cdot 2NaClO_4\cdot 6H_2O$ systems are not available, so the χ_λ factors in our line-strength expressions could not be evaluated. All of the line-strength data reported in this paper are given in units of 10^{-6} D^2/χ_λ.

Chiroptical Spectra. The chiroptical (CD and CPL) spectra measured in this study were used primarily as aids in locating and assigning transitions. Circular dichroic line strengths were not evaluated from the spectra, but the *relative* signs and intensities of the lines observed in these spectra were of crucial importance in making a large number of transition assignments. Recall from eqs 1 and 2 that the requirements for observing CD (or CPL) intensity in a transition are more stringent than those applicable to unpolarized axial absorption (or emission) intensity.

Results and Discussion

Energy Levels. The energy levels located and assigned from our optical and chiroptical measurements (on DyODA at 15 K) are shown in Table 2, along with a listing of all *calculated* energy levels between 0 and 43 000 cm^{-1}. The levels are characterized with respect to their principal ^{2S+1}L term and J-multiplet parentages, their major M_J components, their crystal-field symmetry label (E′ or E″) in the D_3 double-group, and their observed and/or calculated energies. The calculated levels listed in Table 2 were obtained using the Hamiltonian parameter values shown in Table 3. The latter were derived from parametric fits of calculated-to-observed energy-level data, following the procedures described earlier. The number of observed levels included in these data fits was 152, and the number of Hamiltonian parameters allowed to freely vary in performing the fits was 22. Only four of the 26 parameters in the model Hamiltonian were constrained. These parameters were M^2 and M^4, constrained according to $M^2 = 0.56M^0$ and $M^4 = 0.38M^0$, and P^4 and P^6, constrained according to $P^4 = 0.75P^2$ and $P^6 = 0.50P^2$. In Table 3, the *magnitude* of the uncertainty in each parameter value derived from our fits is given in parentheses.

The 152 experimental levels listed in Table 2 only include those crystal-field levels that could be characterized with respect to both location (energy) *and* symmetry (E′ or E″) in our optical absorption and emission experiments. Many more of the 348 levels falling within the spectral range of our measurements (0−43 000 cm^{-1}) were located but could not be unambiguously characterized with respect to symmetry. Only the 152 fully characterized levels were used in our parametric data analyses, and these analyses yielded calculated-to-observed energy-level fits with an rms deviation of 8.2 cm^{-1}. We note from Table 3 that all but one of the Hamiltonian parameter values derived from the data fits are well-determined. Only the three-body configuration-interaction parameter T^4 has an ill-determined value (9 ± 20 cm^{-1}).

In Table 4, we show a comparison of the crystal-field energy parameter (B_m^k) values obtained in the present study for DyODA with those reported previously for other LnODA systems. In that table, we also show values for the "rotational invariant" quantities

$$S^k = (|B_0^k|^2 + 2\sum_{m>0} |B_m^k|^2)^{1/2} \quad (8)$$

which provide useful measures of *crystal-field interaction strengths* (with full rotation-group symmetry).[37] Trans-series plots of the S^4 and S^6 parameter values are shown in Figure 1, along with a listing of S^6:S^4 ratios. The most notable features of the results shown in Table 4 and Figure 1 are (1) the relatively small value of S^2, compared to S^4 and S^6, for *each* of the LnODA systems and (2) the general decrease in S^4 and S^6 values across the series of LnODA systems *except* for the apparently anomalous behavior of GdODA (reflected in the S^4 *and* S^6 parameters) and ErODA (reflected in the S^4 parameter).

(36) Jayasankar, C. K.; Reid, M. F.; Richardson, F. S. *J. Less-Common Met.* **1989**, *148*, 289.

(37) Leavitt, R. P. *J. Chem. Phys.* **1982**, *77*, 1661.

Table 2. Calculated and Experimentally Observed Crystal-Field Levels of Dy^{3+} in $Na_3[Dy(oda)_3]\cdot 2NaClO_4\cdot 6H_2O$

level no.	term[a]	$2J$[a]	$\|2M_J\|$[a]	Γ[b]	energy/cm^{-1} calc[c]	expt[d]	Δ[e]	level no.	term[a]	$2J$[a]	$\|2M_J\|$[a]	Γ[b]	energy/cm^{-1} calc[c]	expt[d]	Δ[e]
1	^{6}H	15	9	E″	−1	0	−1	60	^{4}I(3)	15	13	E′	21978	21988	−10
2	^{6}H	15	11	E′	16	18	−2	61	^{4}I(3)	15	11	E′	22030	22036	−6
3	^{6}H	15	7	E′	30	38	−8	62	^{4}I(3)	15	9	E″	22040	22050	−10
4	^{6}H	15	13	E′	137	129	6	63	^{4}I(3)	15	5	E′	22127	22124	3
5	^{6}H	15	5	E′	177	169	8	64	^{4}I(3)	15	3	E″	22180	22161	19
6	^{6}H	15	15	E″	185	183	2	65	^{4}I(3)	15	1	E′	22187	22180	7
7	^{6}H	15	3	E″	263	273	−10	66	^{4}I(3)	15	7	E′	22273	n.d.	
8	^{6}H	15	1	E′	315	325	−10	67	^{4}I(3)	15	15	E″	22308	22295	13
9	^{6}H	13	11	E′	3527	3520	7	68	^{4}G(4)	11	11	E′	23373	23384	−11
10	^{6}H	13	7	E′	3553	3546	7	69	^{4}G(4)	11	1	E′	23426	n.d.	
11	^{6}H	13	9	E″	3557	3561	−4	70	^{4}G(4)	11	3	E″	23431	23440	−9
12	^{6}H	13	5	E′	3619	3615	4	71	^{4}G(4)	11	5	E′	23444	23451	−7
13	^{6}H	13	1	E′	3630	3629	1	72	^{4}G(4)	11	9	E″	23467	n.d.	
14	^{6}H	13	3	E″	3634	3634	0	73	^{4}G(4)	11	7	E′	23498	23490	8
15	^{6}H	13	13	E′	3673	n.d.									
								74	^{4}M	21	17	E′	24899	24900	−1
16	^{6}H	11	1	E′	5857	5860	−3	75	^{4}M	21	15	E″	24915	24914	1
17	^{6}H	11	9	E″	5882	5882	0	76	^{4}M	21	13	E′	24920	24925	−5
18	^{6}H	11	11	E′	5892	5893	−1	77	^{4}M	21	5	E′	25030	25031	−1
19	^{6}H	11	3	E″	5946	5940	6	78	^{4}M	21	3	E″	25066	25056	10
20	^{6}H	11	5	E′	5951	5947	4	79	^{4}M	21	1	E′	25090	25083	7
21	^{6}H	11	7	E′	5972	5968	4	80	^{4}M	21	19	E′	25127	n.d.	
								81	^{4}M	21	1	E′	25175	n.d.	
22	^{6}H	9	5	E′	7600	7608	−8	82	^{4}M	21	9	E″	25185	25183	2
23	^{6}H	9	9	E″	7605	7613	−8	83	^{4}M	21	7	E′	25208	n.d.	
24	^{6}H	9	7	E′	7650	7645	5	84	^{4}M	21	21	E″	25270	n.d.	
25	^{6}F	11	9	E″	7712	7707	5								
26	^{6}F	11	5	E′	7771	7764	7	85	^{4}I(3)	13	7	E′	25577	25583	−6
27	^{6}H	9	1	E′	7808	7807	1	86	^{4}I(3)	13	11	E′	25604	25613	−9
28	^{6}F	11	7	E′	7825	7824	1	87	^{4}F(3)	7	3	E″	25635	25628	7
29	^{6}H	9	3	E″	7832	7837	−5	88	^{4}F(3)	7	5	E′	25662	25642	20
30	^{6}F	11	1	E′	7840	7840	0	89	^{4}I(3)	13	3	E″	25665	25660	5
31	^{6}F	11	3	E″	7929	7928	1	90	^{4}I(3)	13	1	E′	25696	25693	3
32	^{6}H	9	5	E′	8003	n.d.		91	^{4}F(3)	7	1	E′	25727	25733	−6
								92	^{4}K(1)	17	9	E″	25758	25769	−11
33	^{6}F	9	7	E′	8939	8944	−5	93	^{4}K(1)	17	7	E′	25767	25771	−4
34	^{6}F	9	9	E″	9010	n.d.		94	^{4}K(1)	17	11	E′	25773	n.d.	
35	^{6}F	9	1	E′	9039	9050	−11	95	^{4}F(3)	7	7	E′	25794	25783	11
36	^{6}F	9	5	E′	9084	9088	−4	96	^{4}K(1)	17	3	E″	25819	25816	3
37	^{6}F	9	3	E″	9093	9102	−9	97	^{4}K(1)	17	7	E′	25822	n.d.	
								98	^{4}K(1)	17	5	E′	25830	n.d.	
38	^{6}H	7	1	E′	9171	9171	0	99	^{4}K(1)	17	1	E′	25863	n.d.	
39	^{6}H	7	5	E′	9218	n.d.		100	^{4}K(1)	17	3	E″	25866	25872	−6
40	^{6}H	7	3	E″	9343	n.d.		101	^{4}K(1)	17	1	E′	25873	n.d.	
41	^{6}H	7	7	E′	9364	9368	−4	102	^{4}K(1)	17	15	E″	25876	25893	−17
								103	^{4}K(1)	17	17	E′	25894	n.d.	
42	^{6}H	5	5	E′	10194	10189	5	104	^{4}K(1)	17	17	E′	25915	25933	−18
43	^{6}H	5	3	E″	10225	10218	7								
44	^{6}H	5	1	E′	10328	10317	11	105	^{4}M	19	1	E′	26138	26143	−5
								106	^{4}M	19	15	E″	26146	26148	−2
45	^{6}F	7	1	E′	10965	10962	3	107	^{4}M	19	17	E′	26160	n.d.	
46	^{6}F	7	3	E″	11021	11031	−10	108	^{4}M	19	13	E′	26231	n.d.	
47	^{6}F	7	5	E′	11062	11069	−7	109	^{4}M	19	15	E″	26279	26283	−4
48	^{6}F	7	7	E′	11084	11096	−12	110	^{4}M	19	17	E′	26317	26321	−4
								111	^{4}M	19	11	E′	26421	26418	3
49	^{6}F	5	1	E′	12394	12388	6	112	^{4}M	19	7	E′	26442	26443	−1
50	^{6}F	5	5	E′	12432	n.d.		113	^{4}M	19	9	E″	26446	26441	5
51	^{6}F	5	3	E″	12443	12440	3	114	^{4}M	19	19	E′	26469	n.d.	
52	^{6}F	3	3	E″	13214	13206	8	115	^{4}P(2)	3	1	E′	27343	27334	10
53	^{6}F	3	1	E′	13218	n.d.		116	^{4}P(2)	3	3	E″	27350	27344	6
54	^{6}F	1	1	E′	13763	n.d.		117	^{6}P	5	5	E′	27377	27384	−7
								118	^{6}P	5	3	E″	27395	27394	1
55	^{4}F(3)	9	7	E′	20972	20960	12	119	^{6}P	5	1	E″	27397	27398	−1
56	^{4}F(3)	9	3	E″	21025	21020	5								
57	^{4}F(3)	9	1	E′	21104	21094	10	120	^{4}I(3)	11	9	E″	27850	27862	−12
58	^{4}F(3)	9	5	E′	21169	21164	5	121	^{4}I(3)	11	5	E′	27859	27854	5
59	^{4}F(3)	9	9	E″	21272	21292	−20	122	^{4}I(3)	11	7	E′	27909	27892	17

Table 2 (Continued)

level no.	term[a]	$2J^a$	$\|2M_J\|^a$	Γ^b	energy/cm^{-1} calc[c]	expt[d]	Δ^e	level no.	term[a]	$2j^a$	$\|2M_J\|^a$	Γ^b	energy/cm^{-1} calc[c]	expt[d]	Δ^e
123	^{4}I(3)	11	1	E′	27929	27928	1	184	^{4}D(2)	5	3	E″	31941	n.d.	
124	^{4}I(3)	11	3	E″	27939	n.d.		185	^{4}D(2)	5	5	E′	31959	n.d.	
125	^{4}I(3)	11	11	E′	27981	27972	9	186	^{4}D(3)	1	1	E′	32036	n.d.	
								187	^{4}D(2)	5	1	E′	32045	n.d.	
126	^{4}M	15	13	E′	28365	n.d.									
127	^{6}P	7	1	E′	28387	28382	5	188	^{4}K(1)	13	1	E′	33055	33041	14
128	^{6}P	7	3	E″	28395	28385	10	189	^{4}K(1)	13	7	E′	33075	33074	1
129	^{6}P	7	5	E′	28404	n.d.		190	^{4}K(1)	13	9	E″	33087	n.d.	
130	^{6}P	7	7	E′	28426	28417	9	191	^{4}K(1)	13	11	E′	33093	33093	0
131	^{4}M	15	9	E″	28440	28447	−7	192	^{4}K(1)	13	3	E″	33102	n.d.	
132	^{4}M	15	11	E′	28460	28462	−2	193	^{4}K(1)	13	13	E′	33112	n.d.	
133	^{4}M	15	5	E′	28572	n.d.		194	^{4}K(1)	13	5	E′	33116	33119	−3
134	^{4}M	15	3	E″	28597	n.d.		195	^{4}H(1)	13	13	E′	33376	n.d.	
135	^{4}M	15	1	E′	28610	n.d.		196	^{4}H	13	9	E″	33396	n.d.	
136	^{4}M	15	7	E′	28670	n.d.		197	^{4}H(1)	13	5	E′	33397	n.d.	
137	^{4}M	15	15	E″	28740	n.d.		198	^{4}H(1)	13	11	E′	33402	33402	0
								199	^{4}H(1)	13	3	E″	33413	n.d.	
138	^{4}I(3)	9	7	E′	29415	29427	−12	200	^{4}H(1)	13	7	E′	33422	n.d.	
139	^{4}F(3)	5	3	E″	29509	29498	11	201	^{4}H(1)	13	1	E′	33473	33476	−3
140	^{4}I(3)	9	5	E′	29542	29547	−5								
141	^{4}F(3)	5	1	E′	29591	29592	−1	202	^{4}F(3)	3	3	E″	33533	n.d.	
142	^{4}I(3)	9	3	E″	29631	29628	3	203	^{4}F(3)	3	1	E′	33535	33528	7
143	^{4}I(3)	9	7	E′	29672	29672	0								
144	^{4}I(3)	9	1	E′	29757	29752	5	204	^{4}D(3)	7	5	E′	33864	n.d.	
145	^{4}I(3)	9	9	E″	29764	n.d.		205	^{4}D(3)	7	3	E″	33892	n.d.	
								206	^{4}D(3)	7	1	E′	33898	n.d.	
146	^{4}M	17	15	E″	29870	29878	−8	207	^{4}D(3)	7	7	E′	33955	n.d.	
147	^{4}M	17	13	E′	29881	n.d.									
148	^{4}M	17	5	E′	29897	n.d.		208	^{4}H(1)	11	11	E′	34093	n.d.	
149	^{4}M	17	3	E″	29926	29943	−17	209	^{4}H(1)	11	7	E′	34113	34120	−7
150	^{4}M	17	1	E′	29958	n.d.		210	^{4}H(1)	11	9	E″	24127	n.d.	
151	^{4}M	17	11	E′	29978	n.d.		211	^{4}H(1)	11	1	E′	34135	n.d.	
152	^{4}M	17	9	E″	29986	n.d.		212	^{4}H(1)	11	3	E″	34150	n.d.	
153	^{4}M	17	7	E′	29988	n.d.		213	^{4}H(1)	11	7	E′	34165	34165	0
154	^{4}M	17	17	E′	30024	n.d.									
155	^{4}M	17	3	E″	30052	n.d.		214	^{4}F(3)	5	1	E′	34200	n.d.	
								215	^{4}H(1)	9	5	E′	34226	n.d.	
156	^{4}G(4)	9	5	E′	30090	n.d.		216	^{4}H(1)	9	9	E″	34231	n.d.	
157	^{4}G(4)	9	1	E′	30137	n.d.		217	^{4}H(1)	9	1	E′	34242	n.d.	
158	^{4}G(4)	9	3	E″	30200	n.d.		218	^{4}L	17	9	E″	34252	n.d.	
159	^{4}G(4)	9	7	E′	30206	n.d.		219	^{4}H(1)	9	7	E′	34257	n.d.	
								220	^{4}L	17	11	E′	34282	n.d.	
160	^{6}P	3	1	E′	30670	30684	−14	221	^{4}L	17	15	E″	34289	n.d.	
161	^{6}P	3	3	E″	30680	30685	−5	222	^{4}L	17	13	E′	34292	n.d.	
								223	^{4}L	17	5	E′	34306	34312	−6
162	^{4}K(1)	15	9	E″	31018	n.d.		224	^{4}H(1)	9	1	E′	34327	n.d.	
163	^{4}K(1)	15	11	E′	31040	n.d.		225	^{4}L	17	3	E″	34331	n.d.	
164	^{4}K(1)	15	7	E′	31054	n.d.		226	^{4}L	17	17	E′	34333	n.d.	
165	^{4}K(1)	15	13	E′	31083	31076	7	227	^{4}F(3)	5	3	E″	34339	n.d.	
166	^{4}K(1)	15	5	E′	31119	31115	4	228	^{4}H(1)	9	7	E′	34356	n.d.	
167	^{4}K(1)	15	15	E″	31141	n.d.		229	^{4}H(1)	9	1	E′	34369	n.d.	
168	^{4}L	19	9	E″	31176	n.d.		230	^{4}F(3)	5	3	E″	34403	n.d.	
169	^{4}L	19	7	E′	31192	n.d.									
170	^{4}L	19	5	E′	31197	n.d.		231	^{4}G(2)	11	11	E′	34720	34706	14
171	^{4}K(1)	15	9	E″	31248	n.d.		232	^{4}G(2)	11	1	E′	34734	n.d.	
172	^{4}L	19	11	E′	31251	n.d.		233	^{4}G(2)	11	3	E″	34765	n.d.	
173	^{4}L	19	19	E′	31275	n.d.		234	^{4}G(2)	11	5	E′	34810	n.d.	
174	^{4}L	19	13	E′	31302	n.d.		235	^{4}G(2)	11	7	E′	34836	n.d.	
175	^{4}L	19	15	E″	31311	31290	21	236	^{4}G(2)	11	9	E″	34842	n.d.	
176	^{4}L	19	17	E′	31312	n.d.									
177	^{4}L	19	1	E′	31327	n.d.		237	^{4}K(1)	11	5	E′	35678	n.d.	
178	^{4}L	19	3	E″	31367	n.d.		238	^{4}K(1)	11	1	E′	35756	n.d.	
179	^{4}L	19	1	E′	31395	n.d.		239	^{4}K(1)	11	3	E″	35764	35766	−2
								240	^{4}K(1)	11	11	E′	35835	n.d.	
180	^{4}G(4)	7	1	E′	31439	n.d.		241	^{4}H(1)	7	5	E′	35855	35846	9
181	^{4}G(4)	7	7	E′	31559	n.d.		242	^{4}H(1)	7	1	E′	35888	35886	2
182	^{4}G(4)	7	3	E″	31566	31565	1	243	^{4}H(1)	7	3	E″	35902	n.d.	
183	^{4}G(4)	7	5	E′	31625	n.d.		244	^{4}H(1)	7	3	E″	35958	n.d.	

Table 2 (Continued)

level no.	term[a]	$2J^a$	$\|2M_J\|^a$	Γ^b	energy/cm^{-1} calc[c]	expt[d]	Δ^e	level no.	term[a]	$2J^a$	$\|2M_J\|^a$	Γ	energy/cm^{-1} calc[c]	expt[d]	Δ^e
245	^{4}H(1)	7	7	E′	35980	35968	12	293	^{4}F(2)	9	7	E′	40576	n.d.	
246	^{4}K(1)	11	1	E′	36040	36065	−25	294	^{4}F(2)	9	5	E′	40599	n.d.	
								295	^{4}F(2)	9	3	E″	40609	n.d.	
247	^{4}G(2)	5	1	E′	36321	36342	−21	296	^{4}F(2)	9	1	E′	40721	n.d.	
248	^{4}G(2)	5	3	E″	36350	n.d.		297	^{4}F(2)	9	9	E″	40739	n.d.	
249	^{4}G(2)	5	5	E′	36399	n.d.									
								298	^{2}L(3)	17	15	E″	40788	n.d.	
250	^{4}L	15	7	E′	36426	n.d.		299	^{2}L(3)	17	13	E′	40795	n.d.	
251	^{4}L	15	3	E″	36436	n.d.		300	^{2}L(3)	17	11	E′	40827	n.d.	
252	^{4}L	15	11	E′	36456	36442	14	301	^{2}L(3)	17	5	E′	40891	n.d.	
253	^{4}L	15	9	E″	36464	n.d.		302	^{2}L(3)	17	3	E″	40914	n.d.	
254	^{4}L	15	1	E′	36464	n.d.		303	^{2}L(3)	17	1	E′	40974	40977	−3
255	^{4}L	15	7	E′	36475	n.d.		304	^{4}I(2)	15	7	E′	41005	n.d.	
256	^{4}L	13	11	E′	36489	n.d.		305	^{4}I(2)	15	9	E″	41026	n.d.	
257	^{4}L	13	3	E″	36491	n.d.		306	^{4}I(2)	15	11	E′	41039	41037	2
258	^{4}L	13	5	E′	36498	36500	−2	307	^{4}I(2)	15	13	E′	41044	n.d.	
259	^{4}L	15	13	E′	36520	n.d.		308	^{2}L(3)	17	9	E″	41064	n.d.	
260	^{4}L	15	15	E″	36523	n.d.		309	^{4}I(2)	15	1	E′	41080	n.d.	
261	^{4}L	15	11	E′	36548	n.d.		310	^{4}I(2)	15	5	E′	41094	n.d.	
262	^{4}L	13	13	E′	36555	36560	−5	311	^{4}I(2)	15	3	E″	41096	n.d.	
263	^{4}L	15	3	E″	36569	n.d.		312	^{2}L(3)	17	17	E′	41115	n.d.	
264	^{4}L	15	1	E′	36588	n.d.		313	^{4}I(2)	15	7	E′	41122	n.d.	
								314	^{4}I(2)	15	15	E′	41149	n.d.	
265	^{4}G(2)	9	9	E″	36636	n.d.									
266	^{4}G(2)	9	1	E′	36646	n.d.		315	^{2}N	21	13	E′	41492	n.d.	
267	^{4}G(2)	9	7	E′	36704	36710	−6	316	^{2}N	21	9	E″	41502	n.d.	
268	^{4}G(2)	9	3	E″	36721	n.d.		317	^{2}M(1)	19	19	E′	41510	n.d.	
269	^{4}G(2)	9	5	E′	36732	n.d.		318	^{2}N	21	11	E′	41525	n.d.	
								319	^{2}N	21	5	E′	41570	n.d.	
270	^{4}H(1)	7	1	E′	37512	n.d.		320	^{2}N	21	3	E″	41570	n.d.	
271	^{4}P(2)	1	1	E′	37529	n.d.		321	^{2}N	21	21	E″	41575	n.d.	
272	^{4}H(1)	7	7	E′	37585	n.d.		322	^{4}F(2)	7	1	E′	41577	n.d.	
273	^{4}H(1)	7	3	E″	37614	n.d.		323	^{2}N	21	1	E′	41583	n.d.	
274	^{4}H(1)	7	5	E′	37676	n.d.		324	^{2}M(1)	19	13	E′	41607	n.d.	
								325	^{4}F(2)	7	7	E′	41624	n.d.	
275	^{4}F(2)	3	1	E′	37791	37794	−3	326	^{2}M(1)	19	17	E′	41633	n.d.	
276	^{4}F(2)	3	3	E″	37809	n.d.		327	^{2}N	21	15	E″	41662	n.d.	
								328	^{2}N	21	17	E′	41666	n.d.	
277	^{2}L(3)	15	13	E′	37954	n.d.		329	^{4}F(2)	7	3	E″	41684	n.d.	
278	^{2}L(3)	15	9	E″	38036	n.d.		330	^{2}N	21	13	E′	41698	n.d.	
279	^{2}L(3)	15	11	E′	38066	n.d.		331	^{2}M(1)	19	9	E″	41701	n.d.	
280	^{2}L(3)	15	5	E′	38203	n.d.		332	^{4}F(2)	7	5	E′	41730	41728	2
281	^{2}L(3)	15	3	E″	38245	n.d.		333	^{2}N	21	19	E′	41758	n.d.	
282	^{2}L(3)	15	1	E′	38262	n.d.		334	^{2}M(1)	19	1	E′	41800	n.d.	
283	^{2}L(3)	15	7	E′	38370	n.d.		335	^{2}M(1)	19	3	E″	41822	n.d.	
284	^{2}L(3)	15	15	E″	38439	n.d.		336	^{2}M(1)	19	5	E′	41834	n.d.	
								337	^{2}M(1)	19	11	E′	41930	n.d.	
285	^{4}P(2)	5	1	E′	38749	38756	−7	338	^{2}M(1)	19	13	E′	41940	n.d.	
286	^{4}P(2)	5	5	E′	38869	38878	−9	339	^{2}M(1)	19	15	E″	41942	n.d.	
287	^{4}P(2)	5	3	E″	38914	n.d.									
								340	^{4}I(2)	13	11	E′	41414	n.d.	
288	^{4}P(2)	3	3	E″	39003	n.d.		341	^{4}I(2)	13	9	E″	42424	n.d.	
289	^{4}P(2)	3	1	E′	39011	39010	1	342	^{4}I(2)	13	7	E′	42427	n.d.	
								343	^{4}I(2)	13	1	E′	42450	42441	9
290	^{4}F(2)	5	1	E′	40382	40379	3	344	^{4}I(2)	13	3	E″	42454	n.d.	
291	^{4}F(2)	5	5	E′	40455	40451	4	345	^{4}I(2)	13	5	E′	42458	n.d.	
292	^{4}F(2)	5	3	E″	40467	n.d.		346	^{4}I(2)	13	13	E′	42486	n.d.	
								347	^{2}P(4)	3	3	E″	42870	n.d.	
								348	^{2}P(4)	3	1	E′	42872	42876	−4

[a] Identifies the *principal* $SLJM_J$ components of the eigenvectors. [b] Irreducible representation (irrep) label in the $\bar{D}_3$ double-group. [c] Calculated by using the Hamiltonian parameter values listed in Table 3. [d] Experimentally determined locations of energy levels, with $1/\lambda$(air) to $1/\lambda$(vacuum) corrections included. Uncertainties in the energy-level locations are ca. ±3 cm^{-1} (on average). n.d. ≡ not determined. [e] Difference between calculated and observed energies.

Spectra. Examples of the spectra measured and analyzed in the present study are shown in Figures 2−4. Figure 2 shows results obtained from both *circularly polarized, axial* absorption measurements and *linearly polarized, orthoaxial* absorption measurements in the $^6H_{15/2} \rightarrow {}^4I(3)_{15/2}$ transition region of DyODA at 15 K. In this figure, A_l and A_r denote decadic absorbances for left- and right-circularly polarized light, respectively, and A_σ and A_π denote decadic absorbances for σ-

Table 3. Energy Parameters for the $4f^9$ Electronic Configuration of Dy^{3+} in $Na_3[Dy(oda)_3]\cdot 2NaClO_4\cdot 6H_2O$

parameter[a]	value[b]/cm^{-1}	parameter[a]	value[b]/cm^{-1}
E_{av}	56086(14)	M^0	3.34(0.11)
F^2	93294(82)	M^2	$0.56M^0$
F^4	65933(145)	M^4	$0.38M^0$
F^6	45624(75)	P^2	687(26)
ζ_{so}	1919(1)	P^4	$0.75P^2$
α	17.5(0.2)	P^6	$0.50P^2$
β	−621(8)	B_0^2	−81(18)
γ	1797(38)	B_0^4	−852(28)
T^2	345(7)	B_3^4	−663(24)
T^3	52(4)	B_0^6	502(34)
T^4	9(20)	B_3^6	792(22)
T^6	−397(14)	B_6^6	742(21)
T^7	393(8)		
T^8	330(5)	N[c]	152
		σ[d]	8.2

[a] Defined according to eqs 4 and 5 in the text. [b] Determined by fitting the experimentally observed energy-level data listed in Table 2. [c] Number of assigned energy levels included in the parametric data fits. [d] Root-mean-square deviation between calculated and observed energies (in cm^{-1}).

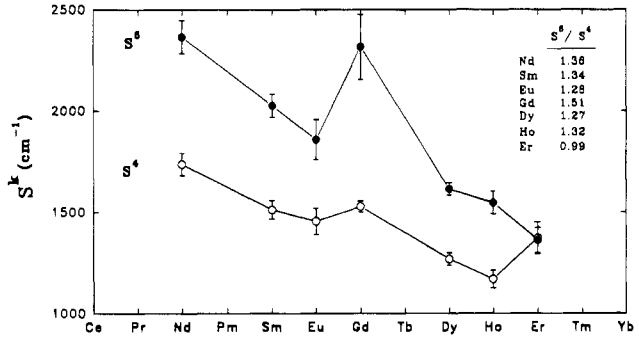

Figure 1. Plots of the S^4 and S^6 crystal-field interaction strength parameters determined for seven LnODA systems. Connecting lines between adjacent data points are included for clarity. Ratios of S^6-to-S^4 parameter values are listed in the upper right-hand part of the figure. See Table 4 for sources of data.

and π- (linearly-) polarized light. The $(A_l - A_r)$ difference spectrum shows the *circular dichroic* (CD) properties of the $^6H_{15/2} \rightarrow {}^4I(3)_{15/2}$ transition region, and the $(A_\sigma - A_\pi)$ difference spectrum shows the *linear dichroic* (LD) properties of this transition region. The spectral peak (or line) numbers in Figure 2 identify the *terminal* crystal-field levels involved in individual transitions (see Table 2 for the energy-level numbering scheme). A single asterisk on a peak number indicates a transition that originates from the first excited crystal-field level of $^6H_{15/2}$ (level 2 in Table 2), and a double asterisk indicates a transition that originates from the second excited crystal-field level of $^6H_{15/2}$ (level 3 in Table 2). Peak numbers *without* asterisks are assigned to transitions that originate from the ground crystal-field level of $^6H_{15/2}$ (level 1 in Table 2). The *unlabeled* features that appear in the $(A_\sigma + A_\pi)$ and $(A_l + A_r)$ spectra of Figure 2 correspond to *vibronic* transitions, an analysis of which lies outside the scope of the present work.

All eight of the crystal-field levels split out of the $^4I(3)_{15/2}$ multiplet of Dy^{3+} ($4f^9$) can be located and assigned (with respect to symmetry type, E′ or E″) from the spectra shown in Figure 2. Five of these levels (numbered as 60, 61, 63, 65, and 66) have E′ symmetry, and the remaining three levels (numbered as 62, 64, and 67) have E″ symmetry. The *ground* crystal-field level of $^6H_{15/2}$ has E″ symmetry (see Table 2), and each transition that originates from this level and terminates on an E″ level of $^4I(3)_{15/2}$ exhibits predominantly π-polarization

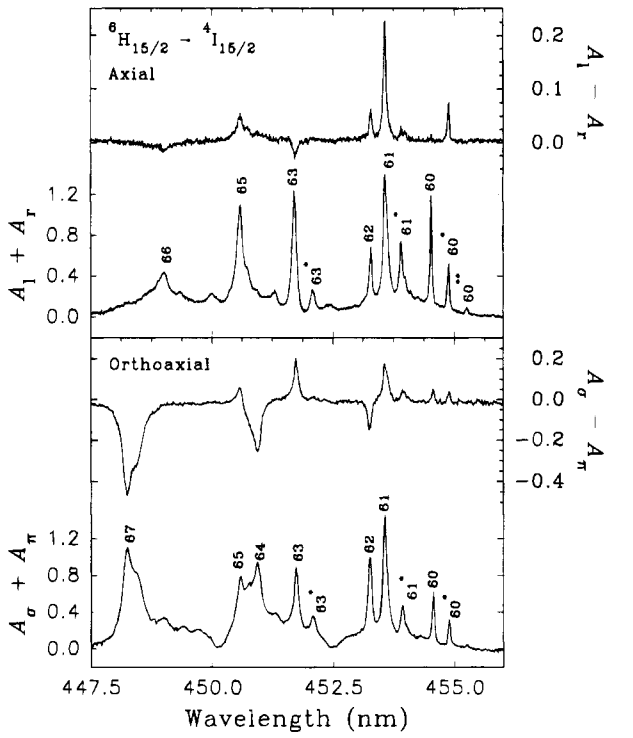

Figure 2. Spectra obtained from circularly polarized, axial absorption measurements (upper frame) and linearly polarized, orthoaxial absorption measurements (lower frame) in the $^6H_{15/2} \rightarrow {}^4I(3)_{15/2}$ transition region of DyODA at 15 K. Each intensity scale is given in decadic absorbance units. The crystal thickness was 0.155 cm in the axial measurements and 0.145 cm in the orthoaxial measurements. See the text for a complete description of the notation used in this figure.

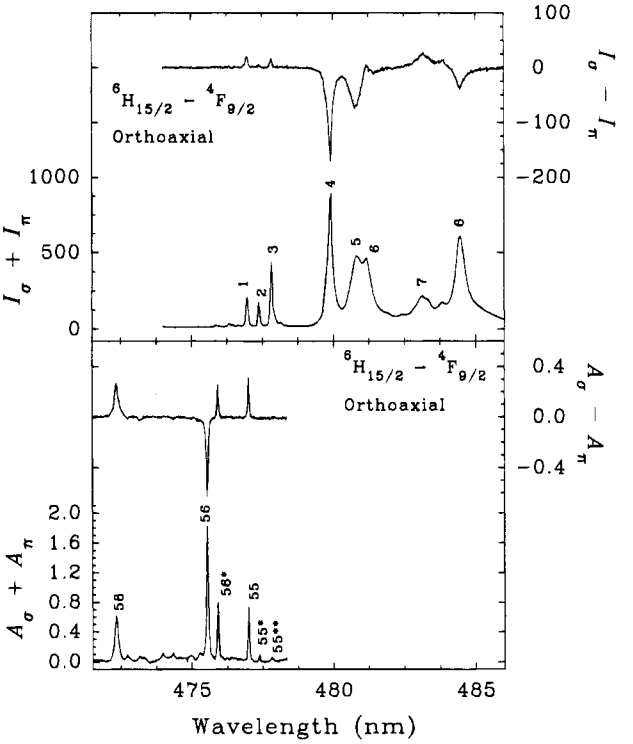

Figure 3. Spectra obtained from linearly polarized, orthoaxial emission (upper frame) and absorption (lower frame) measurements in the $^6H_{15/2} \rightarrow {}^4F(3)_{9/2}$ and $^6H_{15/2} \leftarrow {}^4F(3)_{9/2}$ transition regions of DyODA at 15 K. Crystal thickness was 0.145 cm. See the text for a description of the notation used in this figure.

properties in the orthoaxial absorption spectra. This observation conforms to the *electric-dipole* selection rules given in Table 1 for E″ → E″ transitions.

Table 4. Comparison of Crystal-Field Energy Parameters Determined for $Na_3[Ln(oda)_3]\cdot 2NaClO_4\cdot 6H_2O$ Systems[a]

	values/cm^{-1}						
parameter[b]	NdODA[c]	SmODA[d]	EuODA[e]	GdODA[f]	DyODA[g]	HoODA[h]	ErODA[i]
B_0^2	56(27)	−19(36)	−91(59)	−87(14)	−81(18)	−88(32)	−89(42)
B_0^4	−1111(60)	−941(50)	−947(68)	−952(36)	−852(28)	−836(43)	−881(78)
B_3^4	−943(36)	−837(30)	−781(46)	−845(14)	−663(24)	−578(32)	−745(56)
B_0^6	577(76)	606(54)	411(78)	803(338)	502(34)	531(61)	374(62)
B_3^6	1358(53)	1112(39)	1035(68)	1197(103)	792(22)	777(39)	661(49)
B_6^6	886(68)	794(43)	755(73)	961(24)	742(21)	672(39)	648(37)
S^2	56(27)	19(36)	91(59)	87(14)	81(18)	88(32)	89(42)
S^4	1736(55)	1512(46)	1455(66)	1528(27)	1267(31)	1169(44)	1372(79)
S^6	2365(82)	2025(57)	1858(98)	2315(160)	1615(31)	1547(56)	1361(62)
N	116	144	61	60	152	105	65
σ	14.4	12.3	9.9	6.3	8.2	9.1	9.6

[a] Determined from parametric analyses of empirical energy-level data. N = number of assigned energy levels included in the data fits. σ = rms deviation between calculated and observed energies (expressed in cm^{-1}). [b] The B_m^k crystal-field parameters are defined according to eq 5 in the text. The S^k *crystal-field strength* parameters are defined according to eq 8 in the text. [c] From ref 8. [d] From ref 11. [e] From ref 15 and J. Quagliano (University of Virginia), unpublished results. [f] From ref 20. [g] From present work. [h] From ref 22. [i] From ref 25.

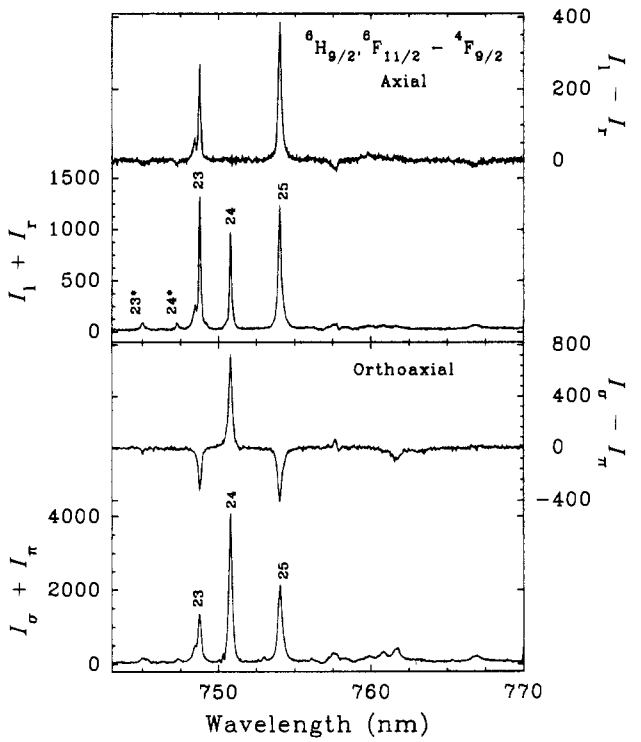

Figure 4. Spectra obtained from circularly polarized, axial emission measurements (upper frame) and linearly polarized, orthoaxial emission measurements (lower frame) in the $^6H_{9/2}$, $^6F_{11/2} \leftarrow {}^4F(3)_{9/2}$ transition region of DyODA at 15 K.

Figure 3 shows results obtained from *linearly polarized, orthoaxial* absorption and emission measurements in the $^6H_{15/2} \rightarrow {}^4F(3)_{9/2}$ and $^6H_{15/2} \leftarrow {}^4F(3)_{9/2}$ transition regions of DyODA at 15 K. In the absorption spectra, the intensity scales are expressed in decadic absorbance units (identical to those used in Figure 2), and in the emission spectra, the σ- and π-polarized emission intensities (denoted by I_σ and I_π, respectively) are expressed in *photon counts*. Peak numberings in the $(A_\sigma + A_\pi)$ spectrum identify terminal crystal-field levels in $^6H_{15/2} \rightarrow {}^4F(3)_{9/2}$ absorptive transitions, and peak numberings in the $(I_\sigma + I_\pi)$ spectrum identify terminal crystal-field levels in $^6H_{15/2} \leftarrow {}^4F(3)_{9/2}$ emissive transitions.

All of the lines observed in the $^6H_{15/2} \leftarrow {}^4F(3)_{9/2}$ emission spectra at 15 K are assigned to transitions that originate from the lowest crystal-field level of the $^4F(3)_{9/2}$ multiplet (level 55 in Table 2). From Figure 3 we note that these lines reveal that relative locations of all eight crystal-field levels split out of the $^6H_{15/2}$ (*ground*) multiplet (levels 1−8 in Table 2). The $^6H_{15/2} \rightarrow {}^4F(3)_{9/2}$ absorption spectra shown in Figure 3 permit the location and assignment of just three of the five crystal-field levels split out of $^4F(3)_{9/2}$ (levels 55, 56, and 58). The remaining two levels (57 and 59) were located from transitions observed in *axial* absorption spectra recorded throughout the $^6H_{15/2} \rightarrow {}^4F(3)_{9/2}$ transition region.

Figure 4 shows results obtained from both *circularly polarized, axial* emission measurements and *linearly polarized, orthoaxial* emission measurements in the $^6H_{9/2}$, $^6F_{11/2} \leftarrow {}^4F(3)_{9/2}$ transition region of DyODA at 15 K. In the axial spectra, $(I_l + I_r)$ and $(I_l - I_r)$ denote, respectively, sums and differences of left- and right-circularly polarized emission intensities (expressed in photon counts). Only the three most intense emission lines in the $(I_l + I_r)$ and $(I_\sigma + I_\pi)$ spectra of Figure 4 are labeled. These lines are assigned to transitions that originate from the lowest crystal-field level of $^4F(3)_{9/2}$ (level 55 in Table 2) and terminate on three adjacent crystal-field levels (numbered as 23, 24, and 25) within the overlapping and intermixed $^6H_{9/2}$ and $^6F_{11/2}$ multiplet manifolds. The lines labeled as 23 and 25 correspond to E″ ← E′ type transitions, whereas line 24 corresponds to an E′ ← E′ type transition. Lines 23 and 25 exhibit predominantly π-polarized character in the orthoaxial spectra, and they also show strong $(I_l + I_r)$ *and* $(I_l - I_r)$ signals in the axial spectra. These observations indicate a dominant *magnetic-dipole* $(m_{\pm 1})$ intensity mechanism for the underlying E″ ← E′ transitions. Line 24, on the other hand, exhibits predominantly σ-polarized character in the orthoaxial spectra, and a strong $(I_l + I_r)$ signal, but no $(I_l - I_r)$ signal, in the axial spectra. These observations for line 24 are compatible with an E′ ← E′ transition that occurs via a predominantly *electric-dipole* $(\mu_{\pm 1})$ intensity mechanism.

The spectra shown in Figures 2−4 illustrate the types of spectroscopic results that were used to locate and assign crystal-field energy levels of Dy^{3+} ($4f^9$) in DyODA. In nearly all of the transition regions of interest, comparisons between axial and orthoaxial measurements and among unpolarized, circularly polarized, and linearly polarized line intensities were essential to making transition assignments and establishing crystal-field energy-level structures.

Transition Line Strengths. Thirty-nine of the transitions observed in the unpolarized axial absorption spectrum of DyODA at 15 K were sufficiently well-resolved to permit

Table 5. Unpolarized Axial Line Strengths Determined for Absorptive Transitions Originating from either the Ground or First Excited Crystal-Field Level of Dy^{3+} in $Na_3[Dy(oda)_3]\cdot 2NaClO_4\cdot 6H_2O$

excited level[a]				axial line strength[c]/
no.	multiplet	Γ	$\bar{\nu}$[b]/cm^{-1}	10^{-6} D^2
55*	$^4F(3)_{9/2}$	E′	21002	11.5
55	$^4F(3)_{9/2}$	E′	20960	2.4
57	$^4F(3)_{9/2}$	E′	21094	0.3
58	$^4F(3)_{9/2}$	E′	21164	8.7
60*	$^4I(3)_{15/2}$	E′	21970	4.1
60	$^4I(3)_{15/2}$	E′	21988	1.6
61*	$^4I(3)_{15/2}$	E′	22018	5.8
61	$^4I(3)_{15/2}$	E′	22036	3.6
63	$^4I(3)_{15/2}$	E′	22124	4.8
65	$^4I(3)_{15/2}$	E′	22180	3.6
68	$^4G(4)_{11/2}$	E′	23384	0.9
71*	$^4G(4)_{11/2}$	E′	23435	1.4
71	$^4G(4)_{11/2}$	E′	23451	0.5
63	$^4G(4)_{11/2}$	E′	23490	0.9
74	$^4M_{21/2}$	E′	24900	3.4
76	$^4M_{21/2}$	E′	24925	2.8
77	$^4M_{21/2}$	E′	25031	3.6
79	$^4M_{21/2}$	E′	25083	7.5
85*	$^4I(3)_{13/2}$	E′	25567	6.9
85	$^4I(3)_{13/2}$	E′	25583	2.3
86	$^4I(3)_{13/2}$	E′	25613	5.0
88	$^4F(3)_{7/2}$	E′	25660	6.2
90*	$^4I(3)_{13/2}$	E′	25675	6.4
90	$^4I(3)_{13/2}$	E′	25693	2.0
123	$^4I(3)_{11/2}$	E′	27928	2.4
125	$^4I(3)_{11/2}$	E′	27972	0.3
138*	$^4I(3)_{9/2}$	E′	29410	9.3
138	$^4I(3)_{9/2}$	E′	29427	9.3
139*	$^4F(3)_{5/2}$	E″	29500	8.0
140	$^4I(3)_{9/2}$	E′	29547	7.5
141	$^4F(3)_{5/2}$	E′	29592	3.8
143*	$^4I(3)_{9/2}$	E′	29654	3.2
143	$^4I(3)_{9/2}$	E′	29672	9.4
165	$^4K(1)_{15/2}$	E′	31076	4.9
166	$^4K(1)_{15/2}$	E′	31115	2.0
188	$^4K(1)_{13/2}$	E′	33041	1.3
189	$^4K(1)_{13/2}$	E′	33074	2.8
191	$^4K(1)_{13/2}$	E′	33093	1.8
194	$^4K(1)_{13/2}$	E′	33119	0.8

[a] Terminal level of absorptive transition, identified according to the level-numbering and -labeling scheme used in Table 2. Asterisks identify transitions that originate from the first excited crystal-field level (no. 2 at 18 cm^{-1} above ground). All other transitions originate from the ground crystal-field level of $^6H_{15/2}$. [b] Observed wavenumber (corrected to vacuum) of the absorptive transition. [c] Line strength determined according to eq 7 of the text, *without* inclusion of the χ_λ correction factor.

quantitative determinations of line strength. The results obtained from these line-strength determinations are given in Table 5.

In several previous studies of LnODA systems,[9,12,15,23] optical line-strength data were analyzed in terms of a parametric model in which, for unpolarized axial measurements, the line strength of a transition A → B is written as

$$S_{AB}(\sigma) = {}^1/_2 e^2 \left| \sum_{\lambda,t,p} A^\lambda_{tp} \sum_{l,q} \langle \lambda l, 1-q | tp \rangle (-1)^q \sum_{a,b} \langle \Psi_{Aa} | U^{(\lambda)}_l | \Psi_{Bb} \rangle \right|^2 + {}^1/_2 \left| \sum_q \sum_{a,b} \langle \Psi_{Aa} | \hat{m}_q | \Psi_{Bb} \rangle \right|^2 \quad (9)$$

where $q = \pm 1$, $\lambda = 2, 4, 6$; $t = \lambda, \lambda \pm 1$; $p = 0, \pm 1, ..., \pm t$; $l = q + p$; $\hat{U}^{(\lambda)}_l$ is an intraconfigurational unit-tensor operator; $\hat{m}_q$ is a magnetic-dipole moment operator; and the A^λ_{tp} are parameters that contain structural and mechanistic details relevant to 4f−4f electric-dipole transition intensity.[27,28] In this expression, Ψ_{Aa} and Ψ_{Bb} denote crystal-field state vectors constructed entirely within an $f^N[SL]JM_J$ angular momentum basis, and the summations $\sum_{a,b}$ are over the degenerate components of levels A and B.

The $\{A^\lambda_{tp}\}$ parameter set in eq 9 must reflect the site symmetry of the lanthanide ions, and for the LnODA systems, where this site symmetry is D_3, the $\{A^\lambda_{tp}\}$ set is restricted to parameters with $(\lambda,t,p) = (2,2,0)$, $(2,3,\pm 3)$, $(4,3,\pm 3)$, $(4,4,0)$, $(4,4,\pm 3)$, $(4,5,\pm 3)$, $(6,5,\pm 3)$, $(6,6,0)$, $(6,6,\pm 3)$, $(6,6,\pm 6)$, $(6,7,\pm 3)$, and $(6,7,\pm 6)$. These parameters are further restricted by the relationship $(A^\lambda_{tp})^* = (-1)^{t+p+1} A^\lambda_{t-p}$, which reduces the number of *independent* A^λ_{tp} parameters to 12 (for systems with D_3 symmetry). In our previous analyses of LnODA optical line-strength data, the 12 independent A^λ_{tp} parameters were chosen to be A^2_{20}, A^2_{33}, A^4_{33}, A^4_{40}, A^4_{43}, A^4_{53}, A^6_{53}, A^6_{60}, A^6_{63}, A^6_{66}, A^6_{73}, and A^6_{76}.

The line-strength data available for analysis in the present study (*i.e.*, the data shown in Table 5) were somewhat more limited than those examined in our previous work on NdODA,[9] SmODA,[12] EuODA,[15] and HoODA.[23] These data could be fitted to eq 9 to produce reasonable agreement between calculated and observed line strengths, but the data set was too small to permit definitive exploration of the complete A^λ_{tp} parameter space. More DyODA line-strength data are needed before the A^λ_{tp} intensity parameters for this system can be satisfactorily determined and compared with those of other LnODA systems.

Chiroptical Activity. Several of the transition regions examined in this study exhibit a remarkable degree of natural optical activity (often referred to a *chiroptical activity*). A useful measure of the degree of chiroptical activity in an absorptive transition is given by

$$g_{ab} = \frac{A_l - A_r}{(A_l + A_r)/2} \quad (10)$$

which is called an *absorption* (or *CD/absorption*) *dissymmetry factor*. The analogous quantity for an emissive transition is

$$g_{em} = \frac{I_l - I_r}{(I_l + I_r)/2} \quad (11)$$

which is called an *emission* (or *CPL/emission*) *dissymmetry factor*. These dissymmetry factors are dimensionless quantities that can have values between 2 and −2, but for most electronic transitions in the great majority of optically active (chiral) systems, the magnitudes of these quantities are observed to be <0.01.

Among the transition regions of Dy^{3+} in $Na_3[Dy(oda)_3]\cdot 2NaClO_4\cdot 6H_2O$, the strongest chiroptical activity is observed in the $^6H_{15/2} \rightarrow {}^4I(3)_{15/2}$ *absorption* and $^6H_{11/2}$, $^6H_{9/2}$, $^6F_{11/2} \leftarrow {}^4F(3)_{9/2}$ *emission* regions. The absorption and emission dissymmetry factors determined from CD/absorption and CPL/emission measurements in these regions are shown in Table 6. Note that most of the individual transitions observed in these regions have $|g_{ab}|$ or $|g_{em}|$ values > 0.1, and may be characterized as having a relatively high degree of chiroptical activity. The $|g_{ab}|$ and $|g_{em}|$ values observed in other transition regions are generally at least an order-of-magnitude smaller.

Conclusion

Among all the LnODA systems examined to date, DyODA posed the most difficult challenges for crystal-field energy-level

Table 6. Absorption and Emission Dissymmetry Factors Observed in the $^6H_{15/2} \rightarrow {}^4I(3)_{15/2}$ (*Absorption*) and $^6H_{11/2}$, $^6H_{9/2}$, $^6F_{11/2} \leftarrow {}^4F(3)_{9/2}$ (*Emission*) Transition Regions of Dy^{3+} in $Na_3[Dy(oda)_3]\cdot 2NaClO_4\cdot 6H_2O$

CD/absorption[a]		CPL/emission[b]	
transition[c]	g_{ab}	transition[c]	g_{em}
1 → 60	n.d.	16 ← 55	−0.80
61	0.32	17	0.44
62	0.18	18	−0.23
63	−0.04	19	0.29
64	n.d.	20	−0.18
65	0.09	21	0.70
66	−0.06	22	0.48
67	n.d.	23	0.42
		24	n.d.
		25	0.64
		26−32	n.d.

[a] Absorption dissymmetry factor defined as $g_{ab} = (A_l - A_r)/[(A_l + A_r)/2]$. n.d. ≡ not determined. [b] Emission dissymmetry factor defined as $g_{em} = (I_l - I_r)/[(I_l + I_r)/2]$. n.d. ≡ not determined. [c] Initial and final levels identified according to the numbering scheme used in Table 2.

location, assignment, and analysis. The $4f^9(Dy^{3+})$ electronic state structure in DyODA is relatively dense, and there are extensive mixing and overlapping between and among different multiplet manifolds. Location and assignment of crystal-field levels required use of the full complement of spectroscopic measurements performed in this study: unpolarized, linearly polarized, and circularly polarized optical absorption and emission measurements on single-crystal samples. The 152 levels located and assigned from these measurements provided a more than adequate basis for an analysis of $4f^9(Dy^{3+})$ state structure between 0 and 43 000 cm^{-1}, which spans 65 $4f^9[SL]J$ multiplet manifolds of Dy^{3+} in DyODA. This analysis was carried out using a parametrized model Hamiltonian defined to be fully commensurate with those employed in previous studies of other LnODA systems. The values of the crystal-field interaction parameters obtained from this analysis are well-determined, and they are closely similar to those reported previously for HoODA. This similarity between the crystal-field interaction strengths (and anisotropies) in DyODA and HoODA conforms to expectations based on the adjacency of Dy^{3+} and Ho^{3+} in the lanthanide series and their very similar ionic radii.

Acknowledgment. This work was supported by the U.S. National Science Foundation (NSF Grant CHE-9213473 to F.S.R.).

IC950366Q